Room-Temperature Surface Engineering of $CuInS_2$ Nanocrystals: Synergistic Effects of Ionic Salts and Dodecanethiol for Enhanced Optical Properties

Shivangi Jain, [a] Nidhi Dubey,[a] Bikram Das,[b] Ali Hossain Khan[b] and Suresh Sarkar*[a]

[a] Department of Chemistry, Indian Institute of Technology Jodhpur, Jodhpur, Rajasthan 342037, India

[b] Department of Chemical and Biological Sciences, S. N. Bose National Centre for Basic Sciences, Salt Lake, Kolkata-700 106, India

Corresponding author's email: sarkar@iitj.ac.in

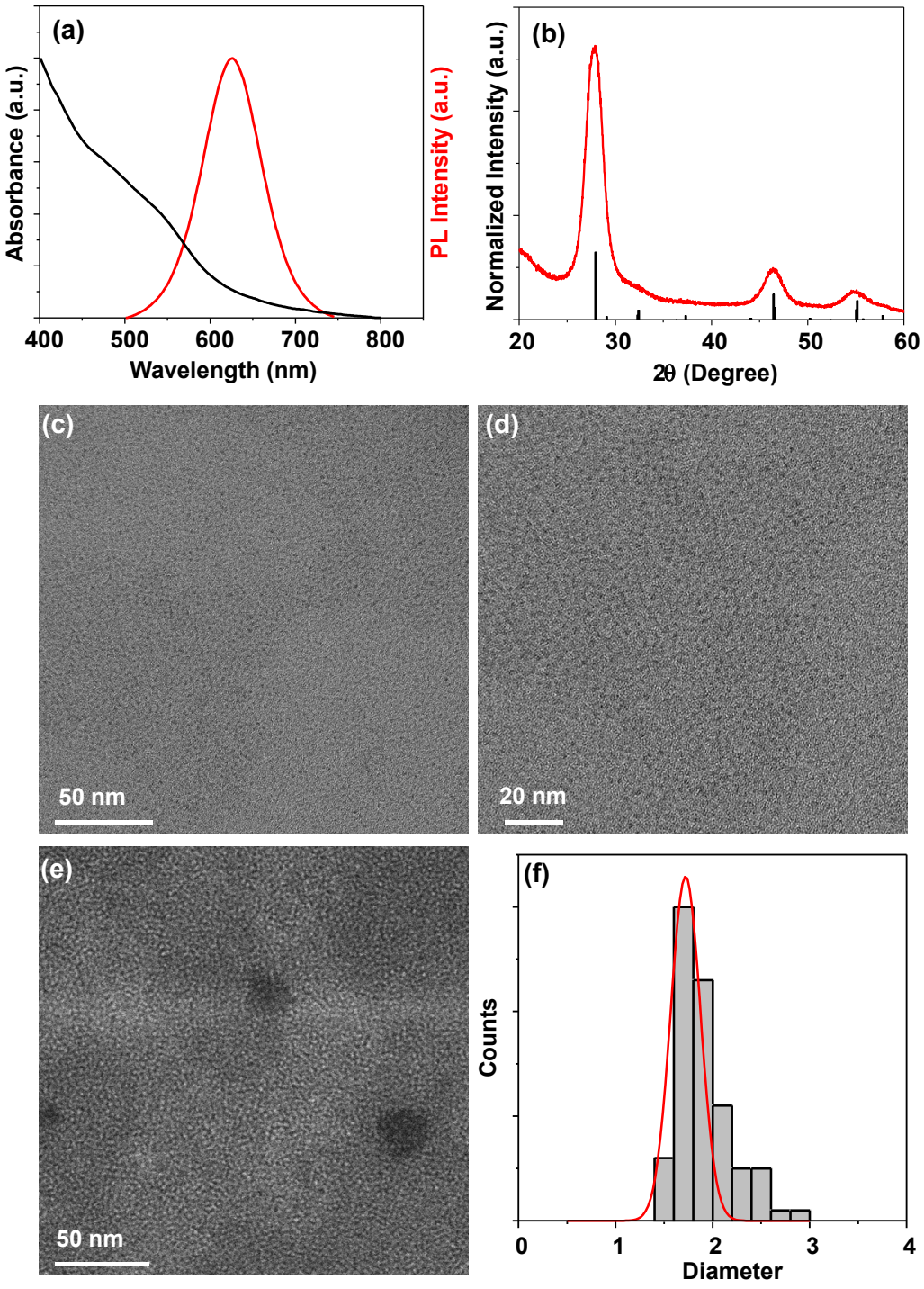

Figure S1. (a) Photoluminescence (PL) and absorption spectra of $CuInS_2$ quantum dots showing emission centered at approximately 625 nm. (b) X-ray diffraction (XRD) pattern confirming the zinc blende phase of the synthesized $CuInS_2$ nanocrystals. The observed XRD pattern matches JCPDS No. 85-1575. (c,d) TEM images at different magnifications showing quasi-spherical, well-dispersed particles. (e) HAADF-STEM image. (f) Size distribution histogram obtained from panel (d) with Gaussian fitting, indicating a narrow size distribution with an average particle size of ~1.7 nm.

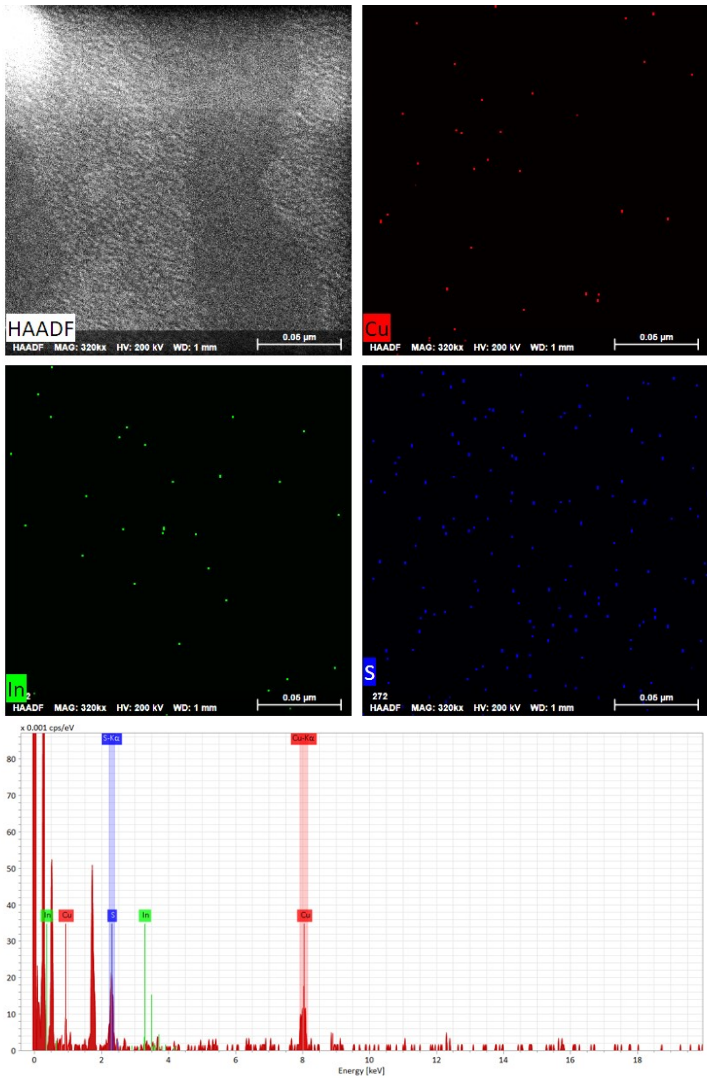

Figure S2. HAADF-STEM image and corresponding elemental mapping of $CuInS_2$ nanocrystals, along with the associated EDS spectrum. The HAADF image (top left) shows the morphology of the nanocrystals, while elemental maps for Cu (red), In (green), and S (blue) confirm the presence and spatial distribution of the constituent elements. Sulfur appears relatively uniformly distributed, whereas Cu and In signals are comparatively less intense and more localized, likely reflecting differences in signal intensity and detection sensitivity. The EDS spectrum exhibits characteristic peaks corresponding to Cu, In, and S, supporting the formation of $CuInS_2$. It should be noted that these TEM-based EDS measurements were acquired using a copper grid, which contributes to the Cu signal and therefore precludes reliable quantitative compositional analysis. As such, the present data provide only qualitative confirmation of elemental composition. To obtain more reliable compositional information, EDS analysis was additionally performed using SEM on a silicon substrate, and quantitative elemental ratios were determined by ICP analysis, as discussed in the main manuscript.

Figure S3. Typical photograph under UV light showing the formation of a biphasic system upon dispersing $CuInS_2$ quantum dots in toluene and introducing methanol and trioctylphosphine (TOP) as a polar phase along with the metal salt.

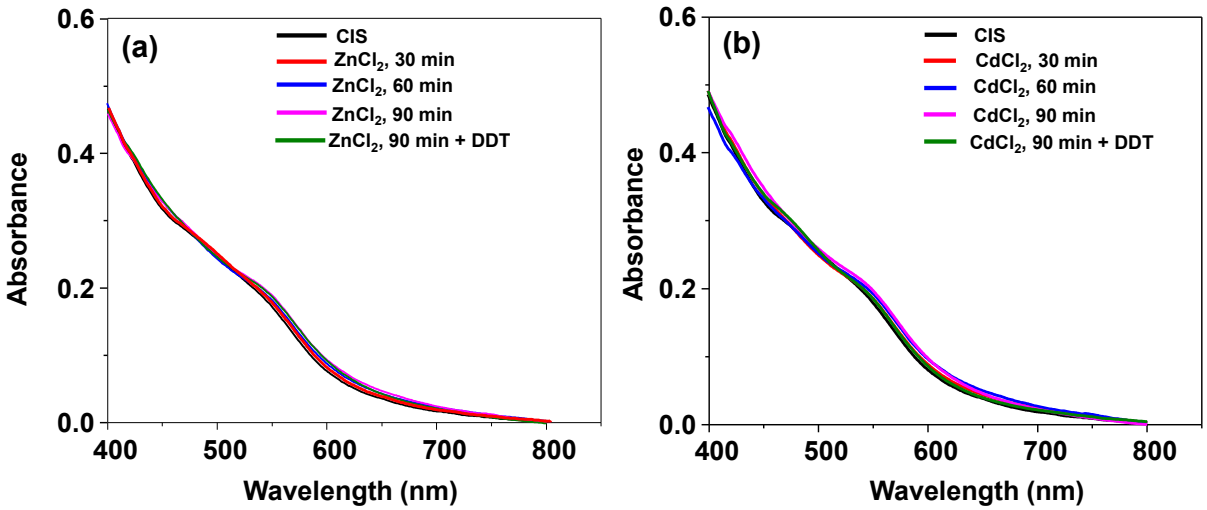

Figure S4. UV–visible absorption spectra recorded at different reaction times (30, 60, and 90 min) during treatment of $CuInS_2$ quantum dots (emitting at 625 nm) with Zn^{2+} and Cd^{2+}, followed by dodecanethiol addition. (a) Zn-treated samples showing no significant shift or change in absorption profile compared to pristine $CuInS_2$. (b) Cd-treated samples also exhibiting nearly identical spectral features across all reaction durations, indicating no alteration in absorption behavior over the course of the reaction.

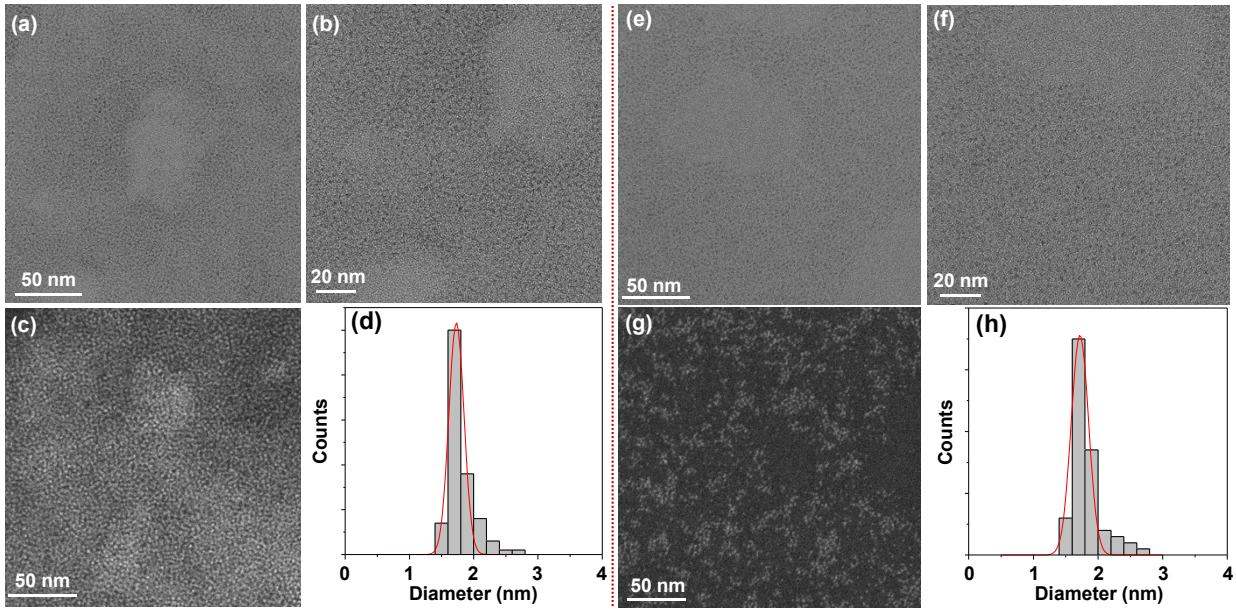

Figure S5. (a,b) TEM images at different magnifications of $CuInS_2$ nanocrystals treated with $ZnCl_2$ followed by DDT, showing quasi-spherical and well-dispersed particles. (c) Corresponding HAADF-STEM image. (d) Particle size distribution histogram derived from panel (b) with Gaussian fitting, indicating a narrow size distribution with an average particle size of ~1.7 nm. (e,f) TEM images at different magnifications of $CuInS_2$ nanocrystals treated with $CdCl_2$ followed by DDT, exhibiting similar quasi-spherical and well-dispersed morphology. (g) Corresponding HAADF-STEM image. (h) Particle size distribution histogram obtained from panel (f) with Gaussian fitting, showing a narrow size distribution with an average particle size of ~1.7 nm.

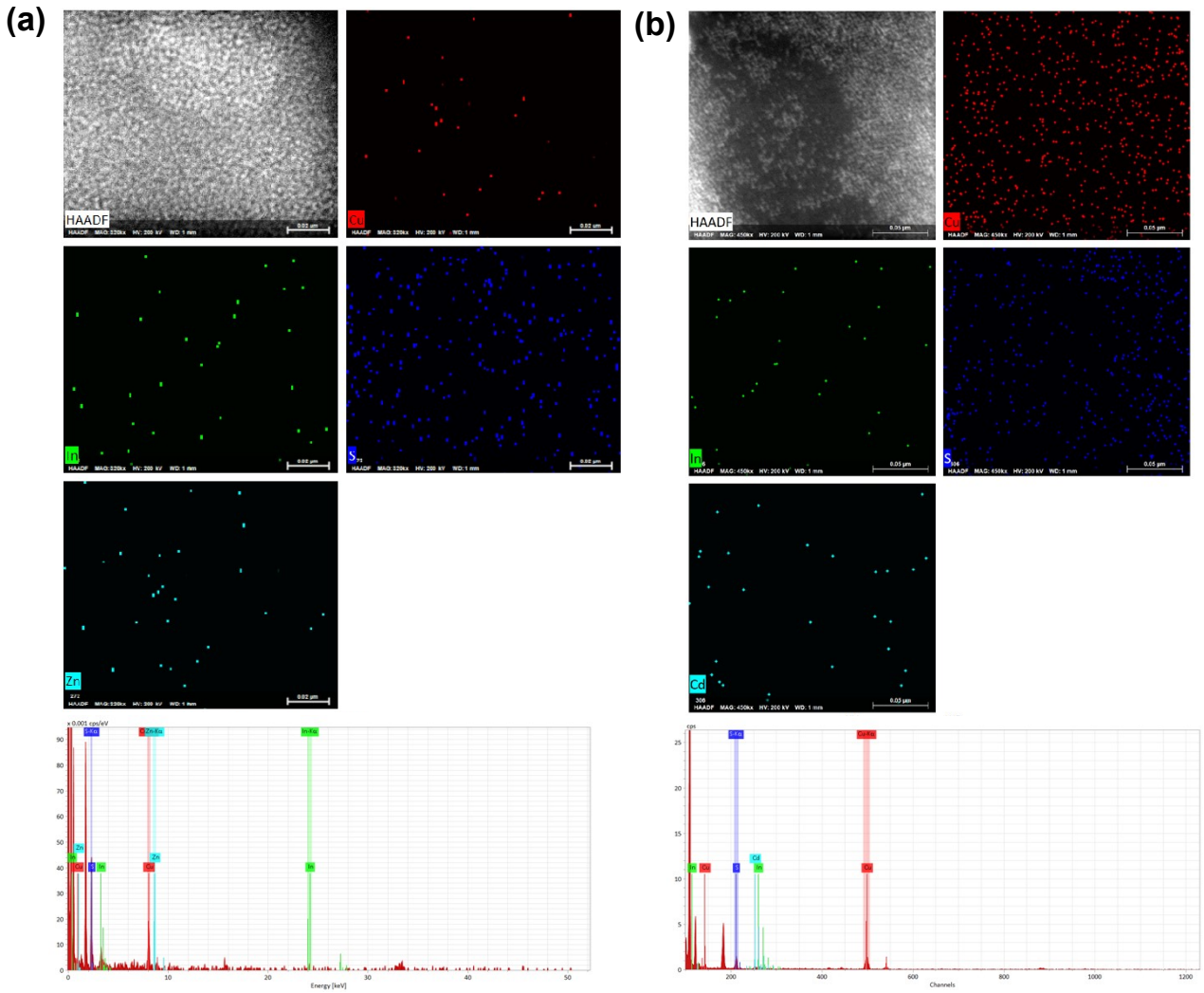

Figure S6. HAADF-STEM images and corresponding elemental mapping of (left) $CuInS_2$/Zn-treated and (right) $CuInS_2$/Cd-treated nanocrystals, along with their associated EDS spectra. The HAADF images (top left in each panel) show the morphology of the nanocrystals. Elemental maps for Cu (red), In (green), and S (blue) confirm the presence of the $CuInS_2$ host lattice. Additional elemental maps for Zn (cyan, left panel) and Cd (cyan, right panel) indicate the incorporation of these cations at or near the nanocrystal surface following post-synthetic treatment with $ZnCl_2$ or $CdCl_2$ in the presence of dodecanethiol. The spatial distribution of Zn and Cd appears relatively sparse and non-uniform compared to sulfur, suggesting surface adsorption or partial shell growth rather than the formation of a well-defined, continuous core–shell structure. Such behavior is consistent with prior reports, where metal–thiol complexes formed in situ can lead to surface passivation, cation exchange at the surface, or the formation of a thin, discontinuous ZnS- or CdS-like layer. The corresponding EDS spectra exhibit characteristic peaks for Cu, In, S, and the respective added elements (Zn or Cd), confirming their presence in the nanocrystals. It should be noted that these TEM-based EDS measurements were acquired using a copper grid, which contributes to the Cu signal and therefore precludes reliable quantitative compositional analysis. As such, the present data provide qualitative confirmation of elemental incorporation. For more reliable compositional analysis, EDS measurements were additionally performed using SEM on a silicon substrate, and quantitative elemental ratios were determined by ICP analysis, as discussed in the main manuscript.

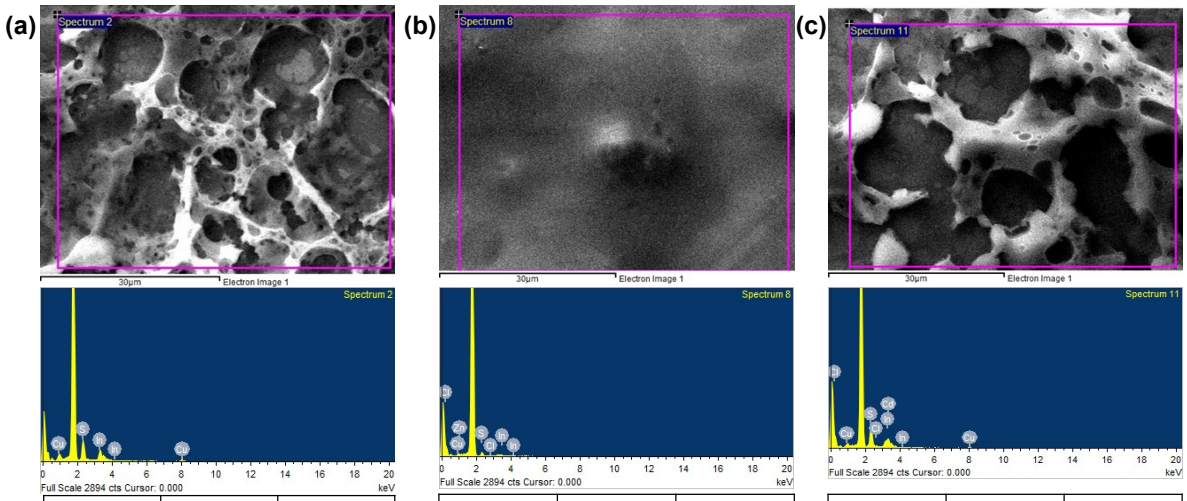

Element	Weight (%)	Atomic (%)
S (K)	32.08	57.57
Cl (K)	1.85	3.00
Cu (K)	15.62	14.14
In (L)	50.46	25.29

Element	Weight %	Atomic %
S (K)	38.65	60.95
Cl (K)	3.33	4.75
Cu (K)	18.00	14.32
Zn (K)	7.07	5.47
In (L)	32.95	14.51

Element	Weight %	Atomic %
S (K)	28.95	54.90
Cl (K)	2.85	4.88
Cu (K)	8.90	8.52
Cd (L)	25.23	13.65
In (L)	34.08	18.05

Figure S7. SEM images and corresponding EDS spectra of (left) $CuInS_2$, (middle) $CuInS_2$/ZnS, and (right) $CuInS_2$/CdS samples. The EDS spectra confirm the presence of the constituent elements, with Cu, In, and S observed in all samples, consistent with the qualitative elemental mapping obtained from HAADF-STEM analysis. Upon surface modification, additional Zn and Cd signals are clearly detected in the $CuInS_2$/ZnS and $CuInS_2$/CdS samples, respectively, confirming successful incorporation of the secondary sulfide phases while retaining the $CuInS_2$ framework. In contrast to TEM-based EDS measurements, where chlorine was not analyzed due to limitations associated with the copper grid and the focus on qualitative mapping, the SEM-EDS analysis performed here additionally includes chlorine detection. A measurable Cl signal is observed; however, its contribution is too low and may originate from residual precursor species rather than firmly bound chloride. Overall, the SEM-EDS results are in good agreement with the TEM elemental mapping, providing complementary confirmation of composition while also offering additional insight into the presence of trace elements such as chlorine.

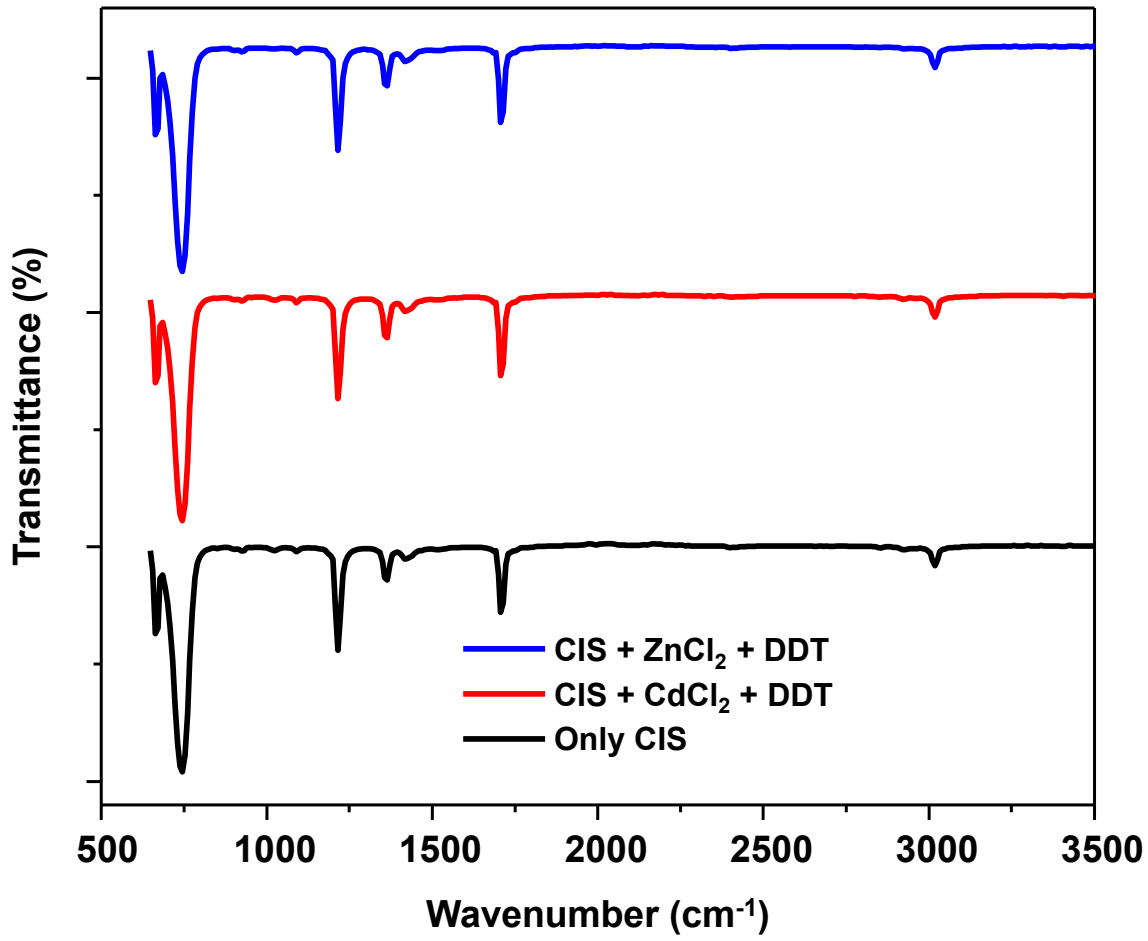

Figure S8. FTIR spectra of DDT-capped $CuInS_2$ nanocrystals before and after $CdCl_2$/DDT and $ZnCl_2$/DDT treatment. The spectra are dominated by DDT ligand vibrations, confirming ligand coverage in all samples. Subtle changes in the ~650–720 cm^{-1} region indicate modification of the thiolate binding environment after treatment. Although FTIR alone does not conclusively demonstrate an increase in dodecanethiol coverage after additional DDT treatment, the observed enhancement in emission suggests that additional adsorption of DDT as surface-bound thiolate is likely, leading to improved passivation of residual surface trap states and reduced nonradiative recombination. Chlorine-related vibrations are not observed, as metal–Cl stretching modes typically appear below ~500 cm^{-1} (often ~300–400 cm^{-1}), outside the measured range, while any weak higher-frequency features (~600–800 cm^{-1}) are likely masked by the strong DDT thiolate and alkyl-chain vibrations.

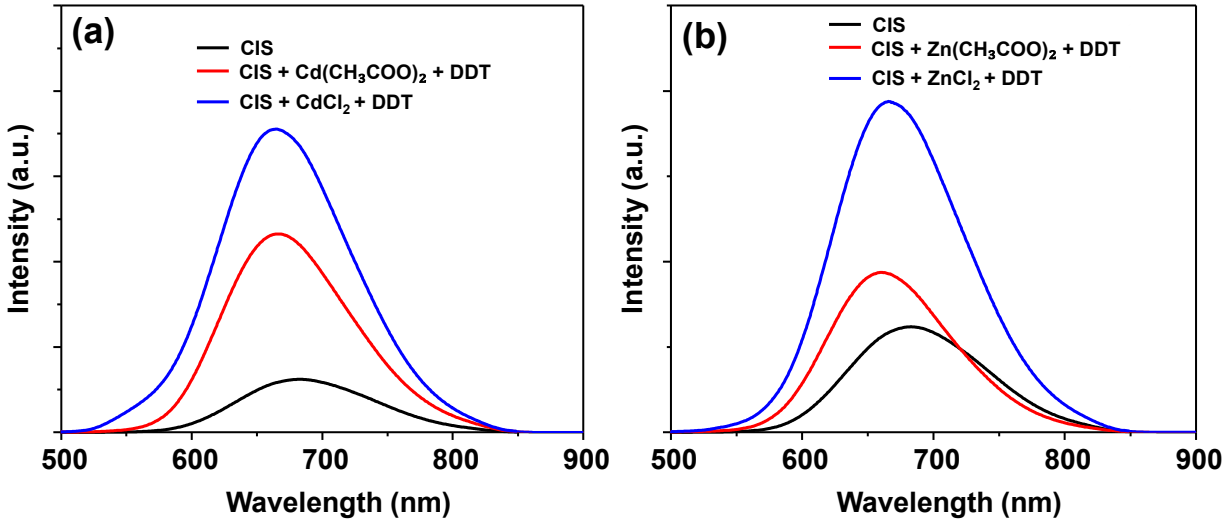

Figure S9. Photoluminescence (PL) spectra of $CuInS_2$ nanocrystals following postsynthetic treatment with different metal precursors and DDT. (a) Comparison of pristine $CuInS_2$ with samples treated using $Cd(CH_3COO)_2$ + DDT and $CdCl_2$ + DDT. (b) Comparison of pristine $CuInS_2$ with samples treated using $Zn(CH_3COO)_2$ + DDT and $ZnCl_2$ + DDT. In both cases, chloride-based treatments (blue) result in a more pronounced enhancement of PL intensity relative to the corresponding acetate-based treatments (red), indicating more effective surface passivation. The observed enhancement is attributed to improved precursor compatibility and reactivity in the methanol/TOP/toluene system, facilitating more efficient defect suppression and ligand-shell reorganization prior to DDT binding. This difference is also attributed to the limited solubility of metal acetates in the methanol/TOP/toluene system, which restricts their interaction with the nanocrystal surface. In contrast, chloride salts enable more effective surface passivation and emission stability, likely through improved precursor availability and transient halide-assisted defect suppression, resulting in enhanced radiative recombination.

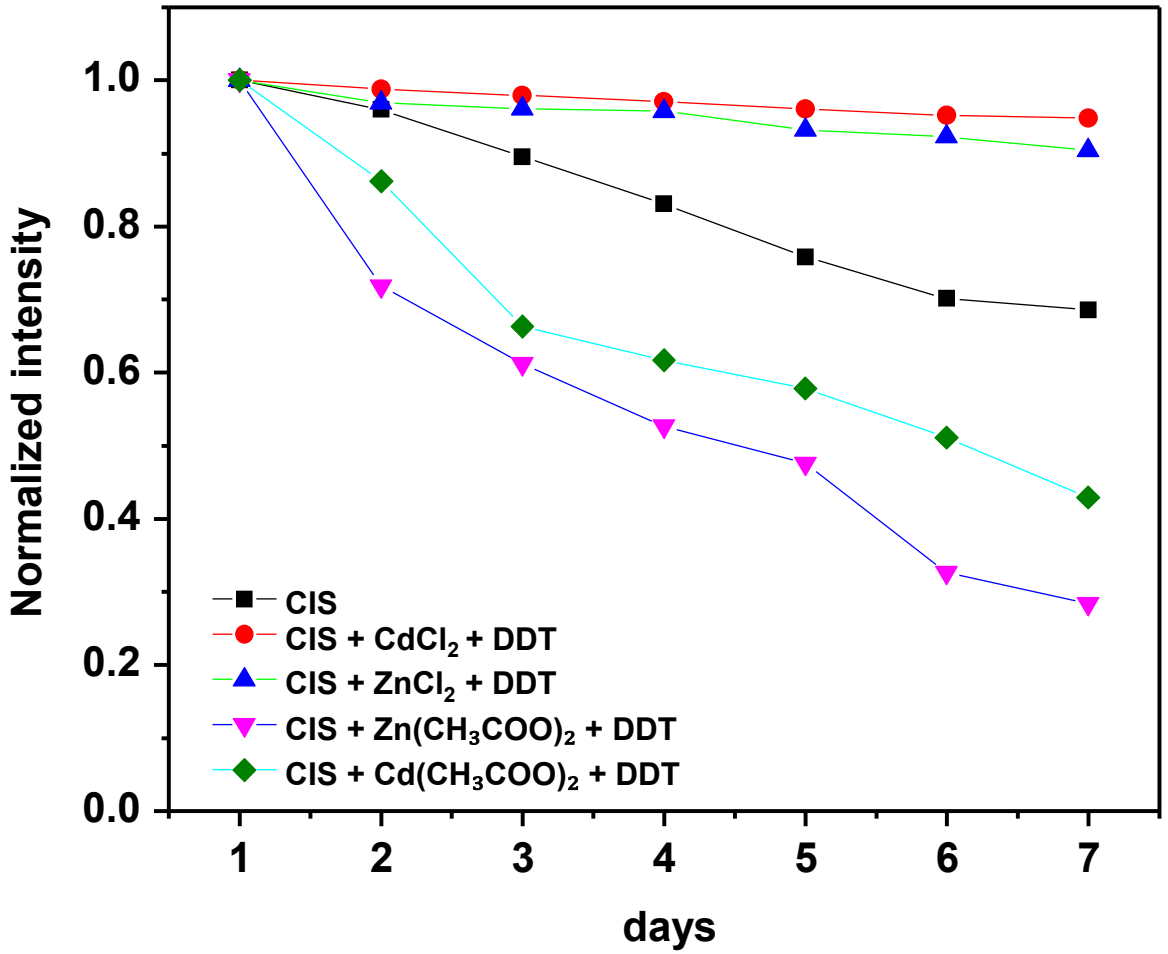

Figure S10. Temporal evolution of normalized PL intensity of $CuInS_2$ nanocrystals following treatment with different metal precursors and DDT. Chloride-derived systems (CdCl2 + DDT and ZnCl2 + DDT) show improved retention of emission intensity compared to acetate-derived counterparts. The observed differences suggest that precursor chemistry influences the effectiveness of surface passivation and the stability of the emissive states. The stability measurements reveal that chloride-treated samples ($CdCl_2$/DDT and $ZnCl_2$/DDT) retain significantly higher PL intensity over time compared to acetate-treated counterparts. This indicates more effective and durable surface passivation, likely arising from improved precursor reactivity and transient halide-assisted defect suppression. In contrast, acetate-based treatments result in faster emission decay, suggesting incomplete passivation and higher susceptibility to nonradiative recombination.

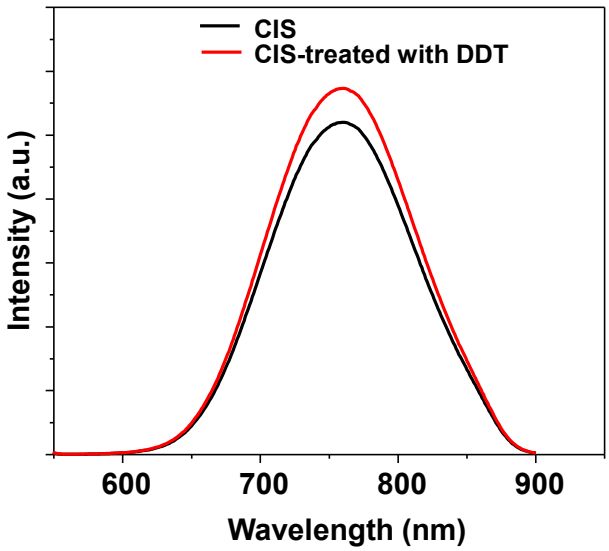

Figure S11. Photoluminescence (PL) spectra of pristine and DDT-treated $CuInS_2$ quantum dots (without any metal salts) recorded under identical excitation conditions. A negligible enhancement in PL intensity is observed after DDT treatment, indicating a limited surface passivation effect in the absence of metal incorporation.

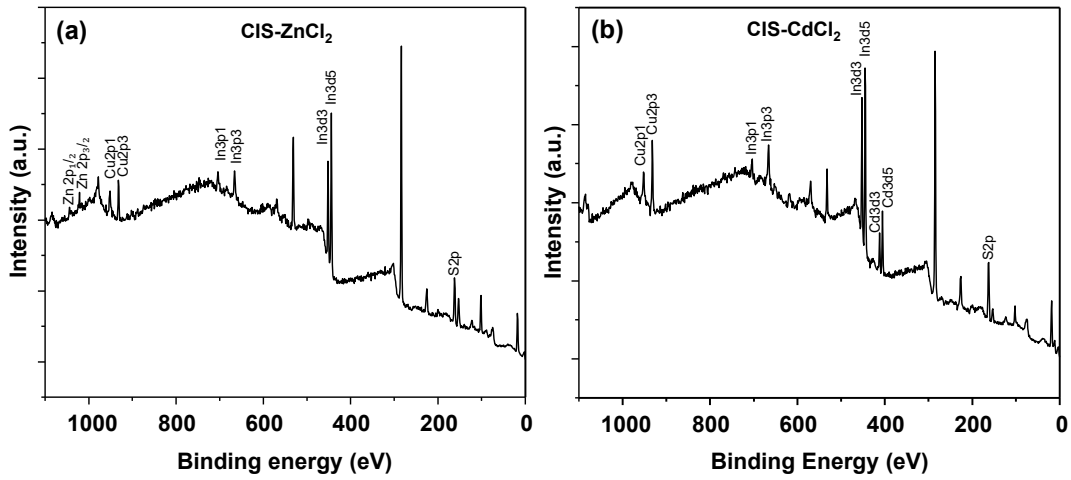

Figure S12. Full-range X-ray photoelectron spectroscopy (XPS) survey scans of (a) Zn^{2+}-treated CIS and (b) Cd^{2+}-treated CIS. The spectra show distinct Zn^{2+} and Cd^{2+} signals, respectively, alongside the characteristic peaks of Cu^{+}, S^{2-}, and In^{3+}.

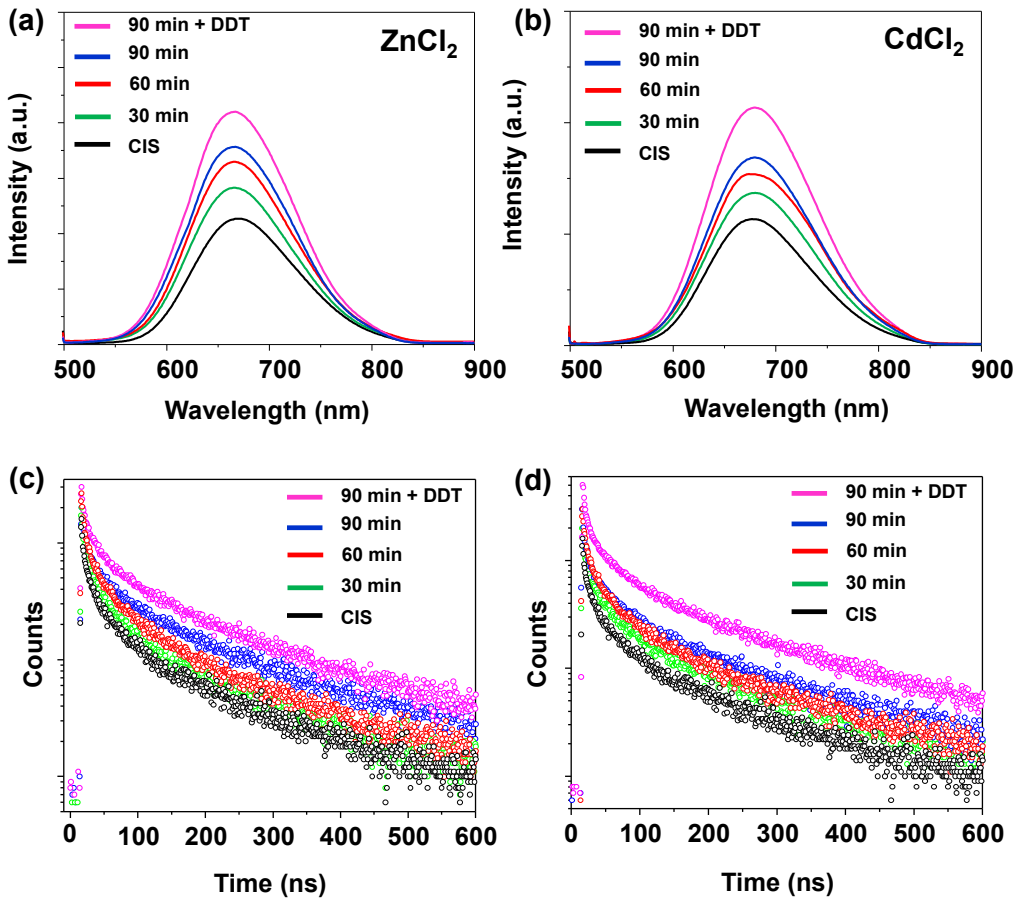

Figure S13. (a) Emission spectra of purified $CuInS_2$ nanocrystals (emitting at 680 nm) and after sequential $ZnCl_2$ treatment followed by thiol capping. (b) Corresponding time-resolved photoluminescence (TRPL) decay curves for the $ZnCl_2$-treated samples (color-matched to panel a). (c) Emission spectra of purified $CuInS_2$ nanocrystals (emitting at 680 nm) and after sequential $CdCl_2$ treatment followed by thiol capping. (d) Corresponding TRPL decay curves for the $CdCl_2$-treated samples (color-matched to panel c). All emission spectra were recorded using an excitation wavelength of 492 nm, while maintaining nearly identical absorbance values at the excitation wavelength for each set of measurements.

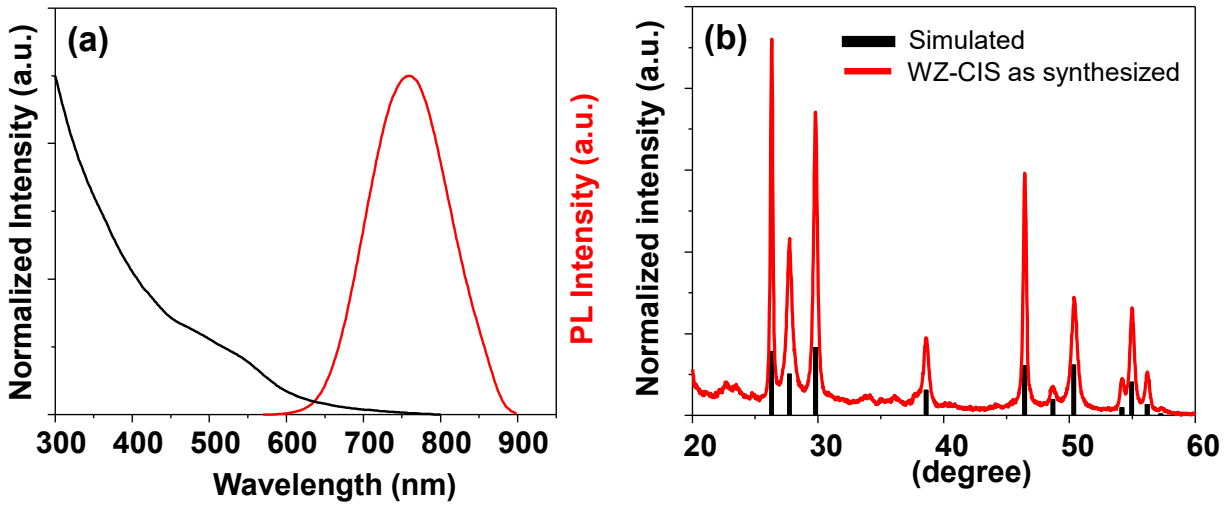

Figure S14. (a) Photoluminescence (PL) and absorption spectra of $CuInS_2$ quantum dots showing emission centered around 758 nm. (b) X-ray diffraction (XRD) pattern confirming the wurtzite phase of the synthesized $CuInS_2$ nanocrystals with indexed diffraction peaks matched with simulated wurtzite phase $CuInS_2$.[1]

Table S1

Respective τ and A values from Figure 1						
	τ1 (ns)	τ2 (ns)	τ3 (ns)	A1	A2	A3
CIS-625	8.95	69.41	251.29	2171.13	1582.36	798.08
$ZnCl_2$, 30 min	12.12	79.04	259.24	2053.086	1593.076	842.2963
$ZnCl_2$, 60 min	9.68	75.45	279.43	2455.609	1509.679	681.6969
$ZnCl_2$, 90 min	10.6	76.2	260.01	1858.665	1369.376	751.1085
$ZnCl_2$, 90 min + DDT	12.02	85.83	285.28	848.9876	635.1066	418.8978
	τ1 (ns)	τ2 (ns)	τ3 (ns)	A1	A2	A3
CIS-625	8.95	69.41	251.29	2171.13	1582.36	798.08
$CdCl_2$, 30 min	9.59	72.82	271.15	3875.641	2436.233	1084.75
$CdCl_2$, 60 min	11.31	77.71	279.55	3371.289	2290.646	1032.86
$CdCl_2$, 90 min	11.5	81.3	292.9	3349.842	2318.1	1053.47
$CdCl_2$, 90 min + DDT	12.05	85.94	285.45	849.1362	634.7498	418.4233

Table S2

Respective τ and A values from Figure 3						
	τ1 (ns)	τ2 (ns)	τ3 (ns)	A1	A2	A3
CIS-758	6.39	50.36	268.47	2289.9285	1783.8159	1755.06
$ZnCl_2$, 30 min	7.83	62.2	307.18	3526.197	2632.0662	2481.6426
$ZnCl_2$, 60 min	7.54	59.32	316.04	4464.9834	3476.6326	3421.1655
$ZnCl_2$, 90 min	7.81	61.61	328.58	5804.8159	4523.1841	4450.1968
$ZnCl_2$, 90 min + DDT	8.27	65.5	351.03	5223.2686	4084.3647	4012.8752
	τ1 (ns)	τ2 (ns)	τ3 (ns)	A1	A2	A3
CIS-758	6.39	50.36	268.47	2289.9285	1783.8159	1755.06
$CdCl_2$, 30 min	7.36	58.24	311.85	5124.9248	4005.9019	3936.3252
$CdCl_2$, 60 min	7.62	60.24	322.5	5996.9727	4685.2266	4604.0488
$CdCl_2$, 90 min	8.03	63.63	340.96	2289.5178	1789.43	1758.3975
$CdCl_2$, 90 min + DDT	8.37	66.2	353.85	6808.7007	5315.0874	5218.8608

References

1. Kruszynska, M.; Borchert, H.; Parisi, J.; Kolny-Olesiak, J., *J. Am. Chem. Soc*., 2010, **132** (45), 15976–15986.